Sensors and Materials, Vol. 36, No. 12 (2024) 5157–5173
MYU Tokyo

S & M 3859

Determination of Influence Line for Shield Tunnel Based on Displacement Response under Passing Train Load Measured Using MEMS Accelerometer

Hidehiko Sekiya,[1*] Kohei Maruyama,[2] and Ikumasa Yoshida[1]

[1]Department of Urban and Civil Engineering, Tokyo City University, 1-28-1 Tamazutsumi, Setagaya 158-8557, Japan
[2]Graduate School of Integrative Science and Engineering, Tokyo City University, 1-28-1 Tamazutsumi, Setagaya 158-8557, Japan

(Received September 24, 2024; accepted November 15, 2024)

Keywords: shield tunnel, influence line, train load, inspection, inverse problem, MEMS accelerometer

Visual inspection and hammering tests are the standard methods for inspecting shield tunnels. They can provide a comprehensive judgment based on the engineer's past experience and conditions, such as cracking, water leakage, and structural details. However, one problem with this method is that the inspection results are highly dependent on the skills of the inspector. To overcome this limitation, it is necessary to develop an easy and quantitative inspection method for shield tunnels. The influence line (IL), which is the response at a specific point due to a unit load that is moved along the target structure, can be used for evaluating the soundness of the infrastructure. Therefore, in this study, we propose a method for determining the IL that can be applied when the speed of a passing train changes. The IL is determined by measuring the displacement due to the train load using a MEMS accelerometer. Finally, to verify the validity of the determined IL, a finite element analysis is performed. Good agreement is found between the ILs determined experimentally and analytically when the soil spring constant is 18 times higher than the nominal value, with a correlation coefficient of 0.98.

1. Introduction

Tunnels can be constructed by mountain tunneling, open-cut tunneling, shield tunneling, or other methods. Tunnels constructed by shield tunneling are called shield tunnels. A typical feature of a shield tunnel structure is that the segments are combined in a ring shape. Shield tunnels in urban areas are important infrastructures that support social and economic activities. With the ongoing development of modern cities, the number of shield tunnels is expected to increase because the above-ground space is limited.[1,2] However, since shield tunnels constructed in the 1950s to 1970s have been in service for more than 50 years, appropriate inspection is essential to ensure their safety and serviceability. The primary defects in shield

*Corresponding author: e-mail: hsekiya@tcu.ac.jp
https://doi.org/10.18494/SAM5376

ISSN 0914-4935
https://myukk.org/

tunnels are cracking and water leakage, and there is concern that these defects will reduce the durability of the segments.[3,4]

Visual inspection and hammering tests are the standard approaches to inspecting shield tunnels. However, while visual inspection and hammering tests can allow a comprehensive judgment based on the engineer's past experience and conditions, such as cracking, water leakage, and structural details, the results strongly depend on the inspectors' skills. There is also an issue that the number of skilled engineers in Japan is decreasing. Therefore, it is necessary to develop an easy and quantitative inspection method for shield tunnels.[5]

Total stations (TSs) are widely utilized for monitoring tunnels that are under construction because accurate displacement information can be obtained between the TS and the target points.[6,7] On the other hand, for an in-service shield tunnel, it is challenging to measure the dynamic response under a train load using a TS because fixed reference points are required, which are not available during train passage.

One approach that does not require fixed reference points is distributed fiber optic sensing (DFOS) for monitoring tunnel deformation and for evaluating the structural health of the shield tunnel.[2,8] DFOS allows distributed long-term strain measurements with millimeter-level spatial resolution.[9,10] However, although it has been shown to be capable of performing dynamic strain measurements,[11] to the best of our knowledge, its applications to shield tunnels have been limited to static strain measurements.

By determining the displacement responses from acceleration records measured using MEMS accelerometers, one of the present authors previously visualized the dynamic deformations of a shield tunnel under a passing train load.[5] Since a MEMS accelerometer does not require a fixed reference point,[12,13] it can be easily installed using adhesive, magnetic jigs, or screws. Furthermore, since a MEMS accelerometer with wireless connectivity does not require wiring,[14–16] field installation is quick and easy. Since sensor installation in shield tunnels must be completed during periods when no trains are passing, easy-to-install sensors such as MEMS accelerometers are highly suitable for measurements in shield tunnels. Furthermore, since the power consumed by MEMS devices is generally low,[17,18] such devices are capable of long-term measurements for infrastructures such as bridges and tunnels.

The displacement response under an external load provides quantitative information for evaluating the soundness of infrastructure.[19–22] However, since the response depends on external loading conditions such as the magnitude of the load and the loading position, in order to evaluate the soundness of a structure, it is essential to convert the response so that it is independent of external loading conditions. Therefore, in structural engineering, the influence line (IL), which is the response at a specific point due to a unit load moved along the target structure, is often used to evaluate the soundness of bridges.[23–27] The IL can be determined from the displacement response and external loading conditions, such as vehicle axle weight and spacing. However, to the best of our knowledge, there have been no studies that determined the IL for a shield tunnel based on displacement data obtained under a train load.

In this study, the IL for a shield tunnel is determined from the displacement under a train load calculated by the double integration of the acceleration measured using a MEMS accelerometer. In previous studies, the speed of an external load such as a traveling vehicle was assumed to be

constant while the vehicle was traveling on the target bridge.[28–30] However, since the target section of the shield tunnel considered in this study is located near a train station, speed changes due to braking occur when the train passes through the target section. Therefore, in this study, we propose a method for determining the IL that can be applied when the speed of a passing train changes. Finally, to verify the validity of the IL determined from the measurement data, a finite element analysis (FEA) was performed using a model for the target tunnel.

The remainder of this paper is organized as follows: In Sects. 2 and 3, we describe the details of the target shield tunnel and an outline of the field measurements, respectively. In Sect. 4, we explain the method for determining the displacement response from acceleration data obtained using a MEMS accelerometer. The formulation used in the conventional calculation method for the IL is summarized in Sect. 5.1, and the proposed methodology for accounting for speed changes of a live load is presented in Sect. 5.2. In Sect. 6, the FEA used to verify the determined IL is described and the FEA results are given. Finally, conclusions and future research are provided in Sect. 7.

2. Target Shield Tunnel

The target shield tunnel and the measurement section are the same as in a previous study.[5] Figure 1 presents a plan view of the target tunnel, which has been in service for about 50 years. It is one of a pair of tunnels, 11.2 m apart, through which trains pass every 2 to 17 min. Although the measurement cross section is a straight tunnel section, there is a nearby curved section in the direction of Futako-tamagawa. In addition, there is a station platform about 180 m away from the measurement section in the direction of Shibuya, as shown in Fig. 1.

A longitudinal section view of the tunnel together with the soil profile is shown in Fig. 2, which gives the standard penetration test N-values for each ground layer in parentheses. The

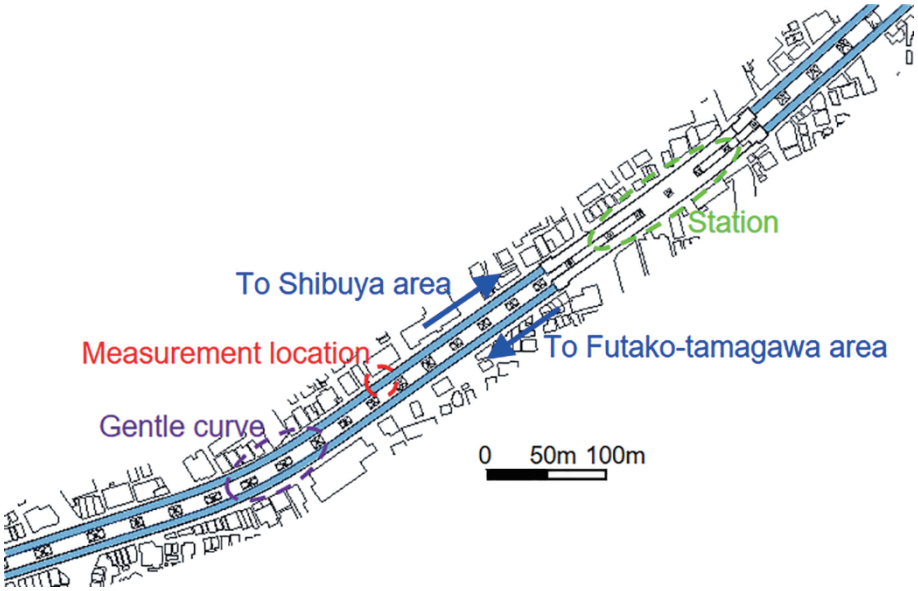

Fig. 1. (Color online) Plan view of target shield tunnel (units: m).

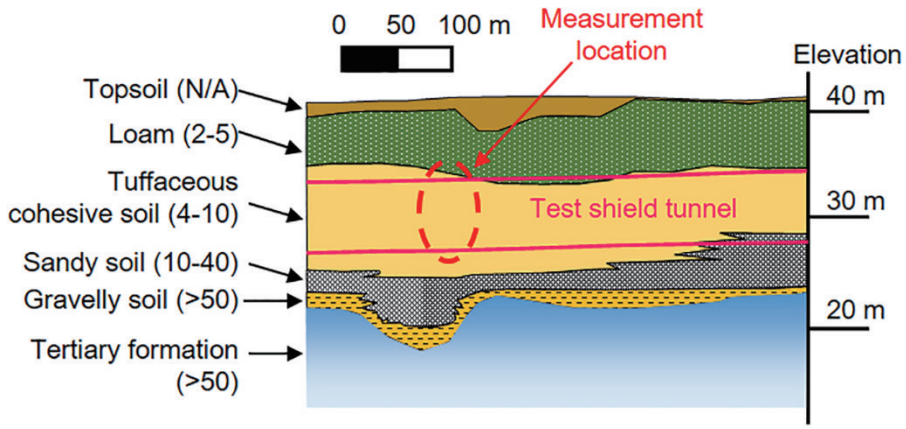

Fig. 2. (Color online) Longitudinal section view of shield tunnel and soil profile (units: m).

target shield tunnel is largely covered by tuffaceous cohesive soil and is located approximately 7 m below ground level.

Figure 3 presents a cross-sectional view of the tunnel, which consists of one K-block and six ribbed reinforced concrete (RC) lining segments. The outer and inner diameters of the tunnel are 6.5 and 5.8 m, respectively.

The detailed dimensions of the ribbed RC lining segments are shown in Fig. 4. All lining segments have the same width of 900 mm and the same thickness of 350 mm.

Figure 5 shows a photograph of the measurement cross section. The blocks are bolted to each other in the cross-sectional and longitudinal directions. K-blocks are alternately located on either side along the longitudinal direction. Although no serious damage was found at the measurement cross section, the water leakage observed was more severe than that at other locations, as shown in Fig. 5. The concrete mixing proportions and specifications for the materials used for the steel bolts and for the steel reinforcement are listed in Tables 1–3, respectively. Further details of the target shield tunnel are given in Ref. 5.

3. Outline of Field Measurements: MEMS Accelerometer

The location of the MEMS accelerometer used for displacement measurements is shown in Fig. 3; the measurement direction is the vertical direction in the figure. Figure 6 presents photographs of the field measurement setup. The MEMS accelerometer was installed using screws and a steel plate on the concrete bottom of the shield tunnel. Note that although several MEMS accelerometers were installed, only the one actually used in this study is shown in Fig. 3.

The specifications of the MEMS accelerometer are listed in Table 4. When calculating the displacement response by doubly integrating the measured acceleration data, it is essential to use a high-resolution accelerometer with a low sensor self-noise density. This is because errors in the measured data, such as quantification errors and sensor self-noise, distort the results of the double integration. In particular, low-frequency errors significantly reduce the accuracy of the displacement response determined by the double integration of acceleration data.[31,32] Therefore,

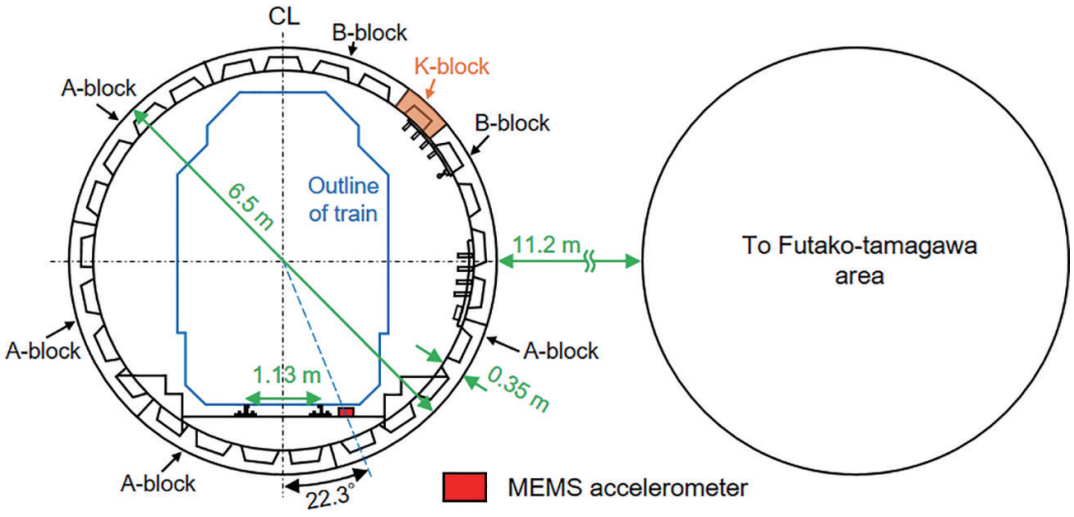

Fig. 3. (Color online) Sectional view of target shield tunnel.

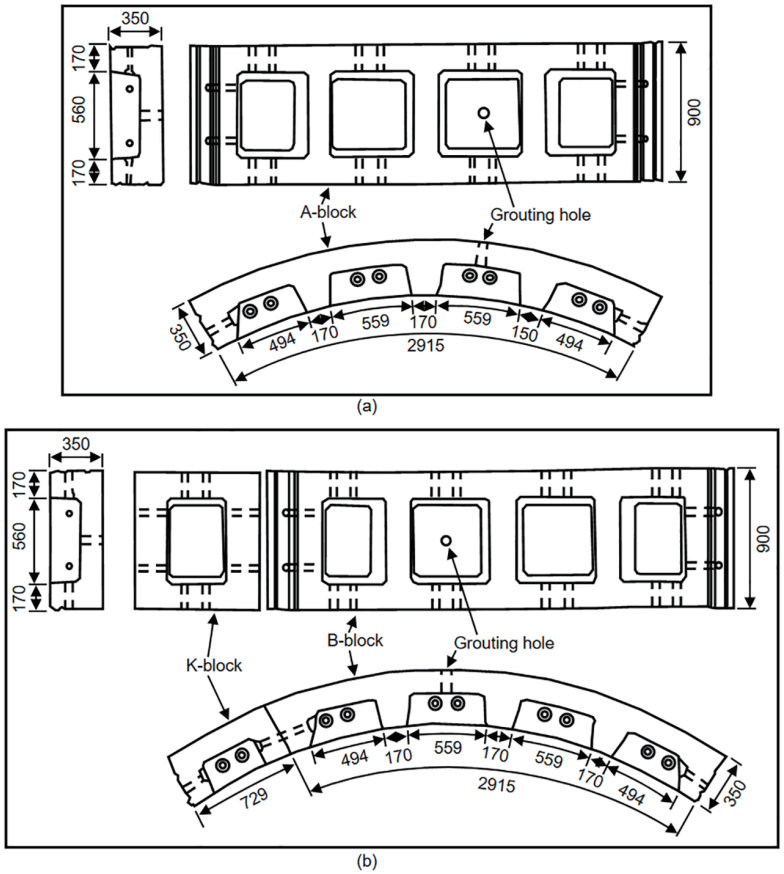

Fig. 4. Dimensions of ribbed RC lining segments (units: mm): (a) A-block and (b) K- and B-blocks.

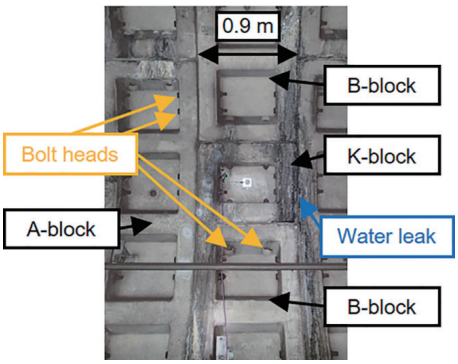

Fig. 5. (Color online) Photograph of measurement cross section.

Table 1
Concrete mixing proportions.

W/C (%)	Design strength (N/mm^2)	G_{max} (mm)	Unit weight (kg/m^3)			
			C	*G*	*W*	*S*
42	47.1	20	390	1218	164	733

C: cement; *G*: coarse aggregate; *W*: water; *S*: fine aggregate.

Table 2
Specifications of steel bolts.

Direction of steel bolts	Diameter (mm)	Steel type	Tensile strength (N/mm^2)	Yield strength (N/mm^2)
Longitudinal and cross-sectional directions	32	SS 41	400	240

Table 3
Specifications of steel reinforcement in lining segments.

External			Internal		
Steel type	Tensile strength (N/mm^2)	Yield strength (N/mm^2)	Steel type	Tensile strength (N/mm^2)	Yield strength (N/mm^2)
SD 30	440–600	295 or more	SR 24	380–520	235 or more

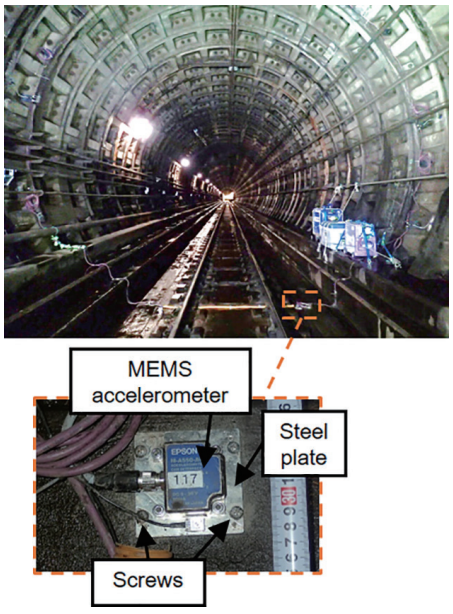

Fig. 6. (Color online) Field measurement setup using MEMS accelerometer.

Table 4
Specifications of MEMS accelerometer.

Model	Noise density [μm/(s^2√Hz)]	Resolution (μm/s^2)	Measurement range (m/s^2)	Frequency bandwidth (Hz)	Dimensions (mm)
M-A550AC2	4.9	0.59	±49.0	20 (−6 dB)	52 × 52 × 26 (width × depth × height)

a quartz-type MEMS accelerometer with a high resolution of 0.59 μm/s^2 and a low noise density of 4.9 μm/(s^2√Hz) was selected in this study. The sampling frequency of the accelerometer was 200 Hz.

4. Determination of Shield Tunnel Displacement from Measured Acceleration

In theory, displacement can be calculated by the double integration of acceleration. However, errors included in the measurement data, particularly those at low frequencies, reduce the accuracy of the calculated displacement.

One of the present authors previously proposed a method for calculating the displacement from the measured acceleration in a shield tunnel.[5] In the proposed method, the acceleration data are divided into those obtained before, during, and after train passage. This shortens the time required for continuous numerical integration and suppresses the loss of accuracy due to measurement errors. It is also assumed that the maximum displacement during the passage of a train is almost constant. This reduces measurement errors caused by external factors, such as shock vibrations, and therefore improves the accuracy of the calculation results. Further details of the proposed method are given in Ref. 5.

Figures 7 and 8 show the acceleration due to a train load measured at the bottom of the shield tunnel using the MEMS accelerometer and the displacement determined from the measured acceleration, respectively.

Although several types of train use the target tunnel, the train that produced the acceleration shown in Fig. 7 can be identified on the basis of the railway timetable. Information on the wheel weights and spacings is shown in Fig. 9. Note that the weights shown in the figure include the additional weight of an assumed number of passengers. Since the train passed during the morning rush hour, the total passenger weight per carriage was calculated under the assumptions listed in Table 5, and the total passenger weight was assumed to be shared equally among the four wheels of each carriage.

In Fig. 8, it can be seen that the displacement response due to the first wheel of the leading carriage begins to occur at about 0.9 s, the response gradually increases in strength, and then suddenly increases at around 3.1 s. From the characteristics of the displacement response, it is considered that the IL for this shield tunnel shows a sharp response when the load is just above the observation point.

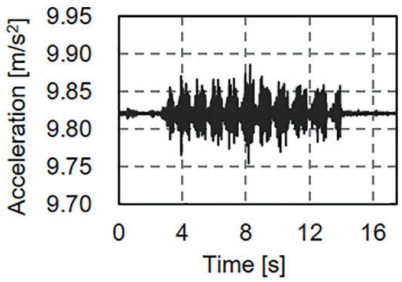

Fig. 7. Acceleration data at bottom of shield tunnel under train load measured using MEMS accelerometer.

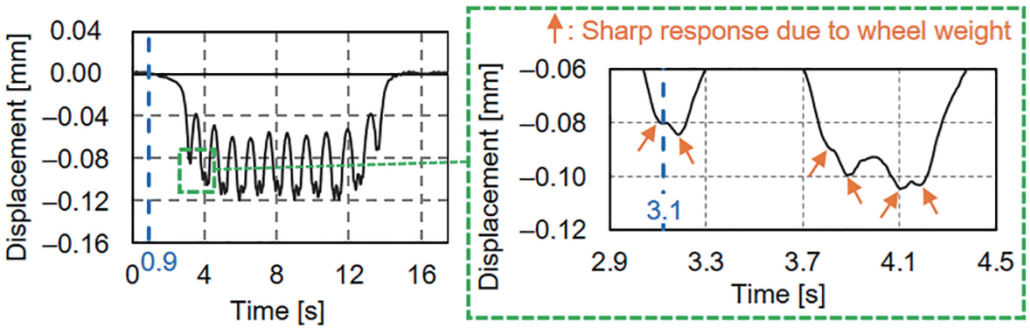

Fig. 8. (Color online) Displacement response calculated from measured acceleration data.

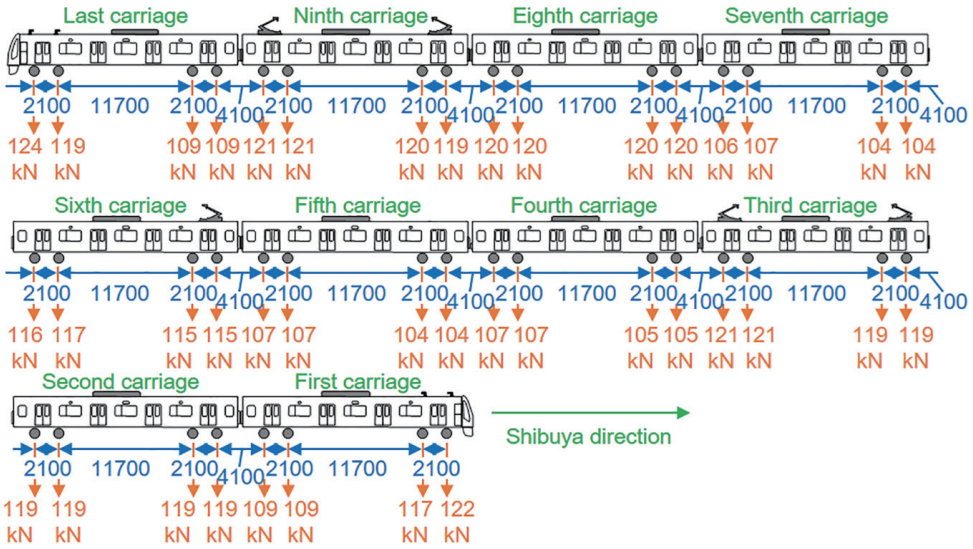

Fig. 9. (Color online) Wheel weights and spacings for train (units for length: mm).

Table 5
Assumed passenger conditions for one carriage during morning rush hour.

Number of people	Weight per person (kN)
250	0.64

5. Calculation of IL from Displacement Response in Shield Tunnel

5.1 Formulation

Here, the method used to calculate the IL from the displacement response is explained. The two most common approaches for calculating the IL from the displacement response are the time-domain (TD) and frequency-domain (FD) methods.[33] However, Mustafa *et al.* pointed out that both methods are basically the same when a cyclic assumption is made for the TD method.[30] Therefore, in this study, the IL is calculated using the TD method without a cyclic assumption, because this assumption is not always appropriate for the displacement response.

The displacement due to passing carriages with known wheel weights and spacings can be written in matrix form as[34,35]

$$\boldsymbol{z} = \boldsymbol{H}\boldsymbol{x} + \boldsymbol{v}\,, \tag{1}$$

where $\boldsymbol{z}$ represents the displacement vector, which is determined from the acceleration data, $\boldsymbol{H}$ is a matrix formulated on the basis of loading information for each wheel, $\boldsymbol{x}$ represents the displacement response vector (time history) for moving unit force, which can be converted to IL easily by changing the time increment Δt to the space increment $\Delta t \times s$, Δt is 0.005 s, depending on the sampling frequency (200 Hz), s is the train speed, and $\boldsymbol{v}$ is the observation error vector, i.e., the residual vector between the measured $\boldsymbol{z}$ and the predicted response $\boldsymbol{Hx}$.

Assuming that the wheel weights are W_1, W_2 ... W_{s-1}, W_s, the matrix $\boldsymbol{H}$ is given by

$$\boldsymbol{H} = \begin{bmatrix}
W_1 & 0 & & & \cdots & & & 0 \\
0 & W_1 & & & & & & \\
\vdots & 0 & \ddots & & & & & \vdots \\
0 & & \ddots & \ddots & & & & \\
W_2 & 0 & \cdots & 0 & W_1 & 0 & \cdots & 0 \\
0 & W_2 & & & & \ddots & & \\
\vdots & 0 & \ddots & & & & \ddots & \\
 & & \ddots & \ddots & & & & W_1 \\
W_s & 0 & \cdots & 0 & W_2 & 0 & \cdots & 0 \\
0 & W_s & & & & \ddots & & \vdots \\
\vdots & 0 & \ddots & & & & \ddots & 0 \\
 & & \ddots & \ddots & & & & W_2 \\
0 & \cdots & \cdots & 0 & W_s & & & 0 \\
 & \ddots & & & \ddots & \ddots & & \vdots \\
\vdots & & \ddots & & & \ddots & \ddots & 0 \\
0 & \cdots & \cdots & 0 & \cdots & \cdots & 0 & W_s
\end{bmatrix}. \tag{2}$$

If the size of $\boldsymbol{x}$ and $\boldsymbol{z}$ are n and m, respectively, then $\boldsymbol{H}$ is an $m \times n$ matrix. The matrix $\boldsymbol{H}$ is determined from the axle weights and their spacings, as indicated in Eq. (2).

The objective function J is obtained by taking the sum of the squared residuals between the measured $\boldsymbol{z}$ and the predicted response $\boldsymbol{Hx}$:

$$J = (\boldsymbol{z} - \boldsymbol{Hx})^{\mathrm{T}} (\boldsymbol{z} - \boldsymbol{Hx}) . \tag{3}$$

The solution $\boldsymbol{x}$ that minimizes J must satisfy

$$\frac{dJ}{d\boldsymbol{x}} = -\boldsymbol{H}^{\mathrm{T}} (\boldsymbol{z} - \boldsymbol{Hx}) = 0 . \tag{4}$$

Therefore, solving the following equation yields the solution $\boldsymbol{x}$ for the IL vector:

$$\boldsymbol{x} = (\boldsymbol{H}^{\mathrm{T}} \boldsymbol{H})^{-1} \boldsymbol{H}^{\mathrm{T}} \boldsymbol{z} . \tag{5}$$

5.2 Consideration of train speed change

The method for calculating the IL described above assumes that the speed of the passing carriages is constant. However, since the target section of the shield tunnel is located near a station, the speed changes owing to braking when the train is passing through the target section. Therefore, in this study, by transforming the displacement response on the basis of the train speed, the displacement response at a constant speed is estimated. Figure 10 shows the relationship between the spacing between the first wheel and each other wheel shown in Fig. 9 and the passage time for each wheel. The passages for each wheel are estimated from the small sharp responses in the displacement response curve shown in Fig. 8.

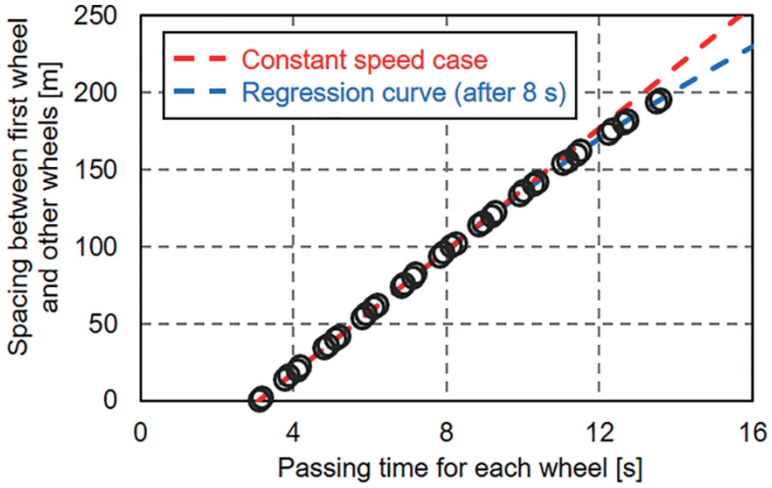

Fig. 10. (Color online) Relationship between spacing between first wheel and other wheels and passage time for each wheel.

From Fig. 10, it can be seen that the carriages pass at a constant speed until around 8 s and then slow down. The relationship between the axle spacing d and the time t after 8 s is obtained by the least-squares fitting of the data points in Fig. 10 using a second-order polynomial:

$$d = -0.4t^2 + 26.5t - 26.0 \cdot \tag{6}$$

By differentiating Eq. (6), it is possible to estimate the speed of the passing carriages at each time point, which is $-0.8t + 26.5$ m/s. On the basis of the estimated speed of the carriages, the displacement response for carriages passing at a constant speed can be determined, as shown in Fig. 11.

The IL determined from the displacement response at a constant speed in Fig. 11 is shown in Fig. 12. The length of the obtained IL is about 40 m. As assumed earlier, the IL for this shield tunnel shows a sharp response when the load is just above the observation point. The measured response $\boldsymbol{z}$ and the predicted response $\boldsymbol{Hx}$ are shown in Fig. 13 and seen to be in generally good agreement.

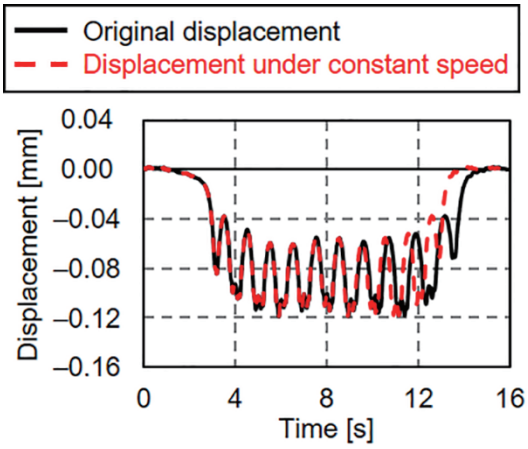

Fig. 11. (Color online) Determined displacement response at constant speed of passing carriage.

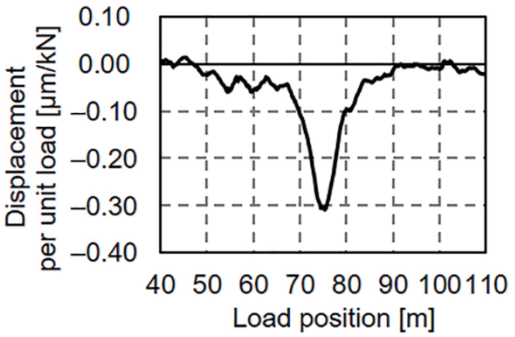

Fig. 12. IL determined from displacement response.

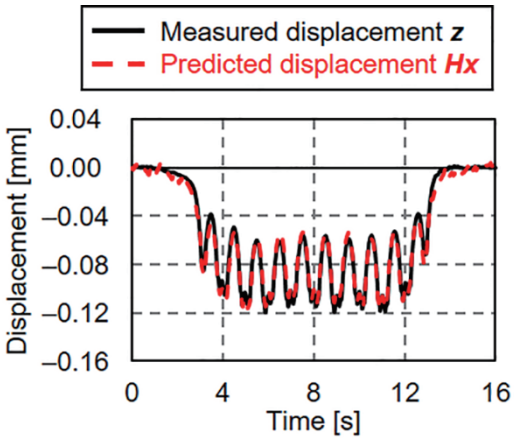

Fig. 13. (Color online) Comparison between measured response z and predicted response $\boldsymbol{Hx}$.

6. FEA for Verification of Determined IL

To verify the IL determined from the displacement response obtained from the acceleration data, a FEA was performed using the ABAQUS 2022 software. Figure 14 shows the finite-element model of a shield tunnel with a length of 150 m.

The RC segments and the concrete floor on which the trains run were modeled using shell elements (S4R) and quadratic tetrahedral solid elements (C3D10), respectively, as shown in Fig. 14(b). The numbers of shell and solid elements are 10200 and 12246, respectively. The outer and inner diameters of the shield tunnel are 6.5 and 5.8 m, respectively, which are the same as those shown in Fig. 3. The segment thickness is 0.35 m, which is the same as that shown in Fig. 4. The thickness and width of the concrete floor are 0.52 and 3.32 m, respectively, as shown in Fig. 14(b). The shield tunnel and the concrete floor are rigidly connected at the contact surface. Since the FE model in this study did not have joints between segments, it was considered that it would be necessary to simulate the effect of joints by reducing the stiffness.[36,37] However, as explained later in this section, since the experimental and analytical results were in good agreement even using the design stiffness, no reduction in stiffness was applied. The reason why the experimental and analytical results were in good agreement even using the design stiffness is believed to be that the actual stiffness of the constructed segments was higher than the design stiffness. Therefore, the input elastic modulus and Poisson's ratio for the RC segments and the concrete floor were set to 38 GPa and 0.17, respectively.

Soil springs were placed at 32 points around the periphery of the shield tunnel to simulate soil reactions corresponding to tunnel deformation, as shown in Fig. 15.[38–40]

All 32 points were constrained by three springs: one normal spring and two shear springs. Therefore, the total number of springs is 96. When analyzing the effects of construction loads, earth pressure, and water pressure, it is assumed that the normal springs do not contribute to tension.[40] However, since the train load is extremely small compared with these loads and the displacement due to the train load is minuscule (about −0.12 mm) as shown in Fig. 8, in this study, the normal springs are assumed to make a linear contribution to both tension and

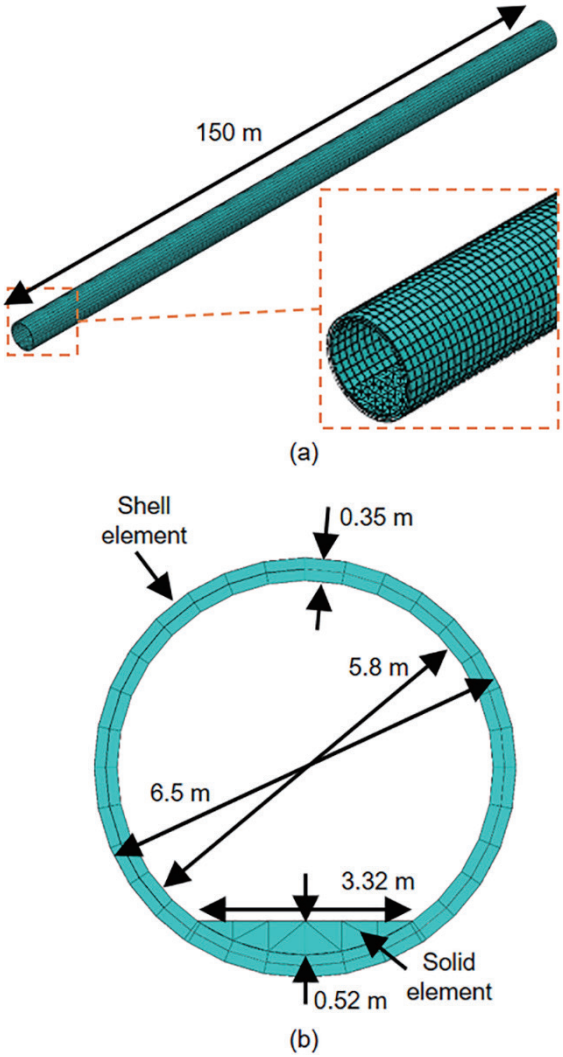

Fig. 14. (Color online) FE model of shield tunnel: (a) overall and (b) cross-sectional views.

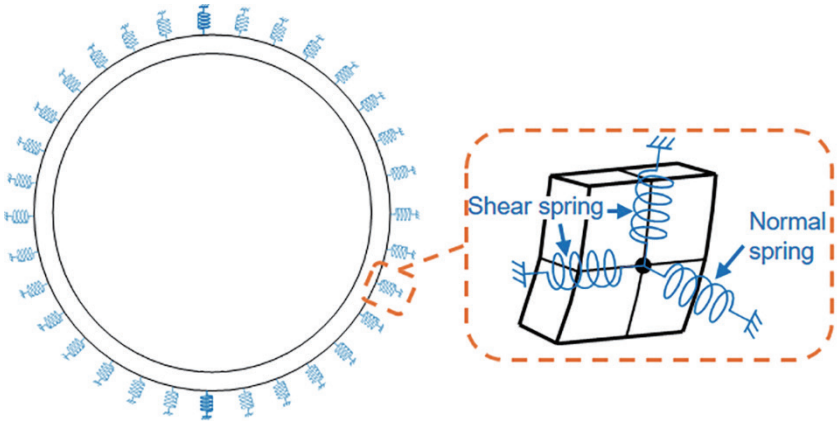

Fig. 15. (Color online) Configuration of soil springs.

compression. As in previous studies, the normal coefficient of subgrade reaction (k_r) was calculated to be 2282 kN/m^3 on the basis of the elastic modulus (E_s) and Poisson's ratio (v) for the soil and the radius (R) of the lining, as expressed in Eq. (7).[41–44]

$$k_r = \frac{3E_s}{(1+v)(5-6v)R} \tag{7}$$

The shear spring constant (k_t), which is 761 kN/m^3 in this study, is assumed to be one-third of the normal spring constant.[45,46]

Because the purpose of the FEA was to obtain the IL, a load of 0.5 N was applied at two locations to give a total load of 1.0 N, as shown in Fig. 16. The distance between the two loads was set to 1.13 m on the basis of the drawing of the target shield tunnel shown in Fig. 3. The two loads were then shifted in steps of 0.5 m along the entire 150 m length in the direction of train travel.

The FEA results are shown in Fig. 17 for different soil-spring constants. The spring constants for both the normal and shear springs were varied by factors of 5, 10, 16, 18, 20, 30, and 100.

Figure. 17(b) shows an enlarged region of Fig. 17(a). Also shown for comparison is the IL determined from the measured displacement response. Since the IL determined by FEM is that at the bottom of the longitudinal center, the maximum displacement response occurs at 75 m (half of 150 m).

As seen in Fig. 17(a), when the spring constant for the soil springs is the same as the nominal value, the IL obtained by FEA is much larger than the measured IL. In Fig. 17(b), it can be seen that the IL obtained by FEA is in good agreement (correlation coefficient of 0.98) with the measured IL when the spring constant is 18 times larger than the nominal value.

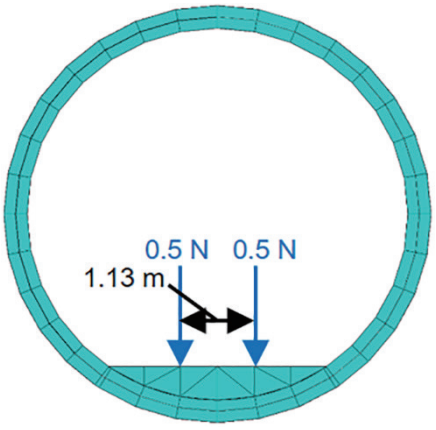

Fig. 16. (Color online) Loading position.

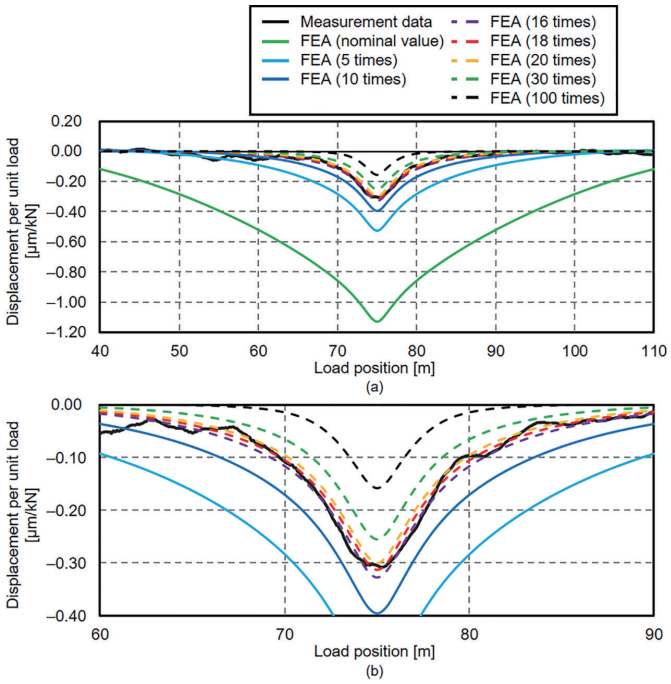

Fig. 17. (Color online) Comparison of ILs obtained by measurement and FEA: (a) all results and (b) enlarged view of (a).

7. Conclusions and Future Research

In this study, in order to develop an easy and quantitative inspection method for shield tunnels, a method was proposed for determining the IL when the speed of a passing train is changing. By the proposed method, the IL for a shield tunnel was determined from the displacement due to a train load, which was calculated from the acceleration measured using a MEMS accelerometer. Such an accelerometer is suitable for this purpose because it is easy to install and does not require a fixed reference point. Finally, a FEA was performed using a model for the shield tunnel in order to verify the validity of the measured IL. The conclusions of this study are as follows:

(1) The proposed method can be used to successfully determine the IL for the shield tunnel even when the speed of a passing train was not constant. It is considered that the determined IL can be used to evaluate the soundness of a shield tunnel.
(2) The determined IL showed a sharp response when the load was just above the observation point, and the length of the obtained IL was about 40 m.
(3) The FEA and measurement results were in good agreement when the spring constant for the soil springs was 18 times larger than the nominal value, with a correlation coefficient of 0.98.

A limitation of the proposed method is that it is applicable only when information is available on the wheel weights and spacings for passing carriages. Therefore, in future research, a method for calculating the IL that does not require such information will be considered. Future studies will examine detectable defects, their extent, and appropriate measurement locations based on the IL. Future studies will also include comparing the results of the proposed method with those

of existing methods such as visual inspection and laser scan. Furthermore, the response of the IL to changes in soil conditions and the shield tunnel structure will be investigated by FEA. In addition, the effects of countermeasures against damage such as cracking and water leakage will also be studied by analyzing the ILs before and after such treatments are performed.

Acknowledgments

The field measurements using MEMS accelerometers were supported by TOKYU RAILWAYS Co., Ltd. and Seiko Epson Co., Ltd.

References

1 M. G. Li, J. J. Chen, J. H. Wang, and Y. F. Zhu: Tunnelling Underground Space Technol. **71** (2018) 329. https://doi.org/10.1016/j.tust.2017.09.014
2 H. H. Zhu, D. Y. Wang, B. Shi, X. Wang, and G. Q. Wei: Tunnelling Underground Space Technol. **124** (2022) 104483. https://doi.org/10.1016/j.tust.2022.104483
3 S. Morimoto, A. Kusaka, T. Ishimura, and N. Isago: Proc. of Tunnel Eng. JSCE. **25** (2015) II-3. http://library.jsce.or.jp/jsce/open/00047/2015/25-02-03.pdf
4 F. Meng, B. Hu, R. Chen, H. Cheng, and H. Wu: Underground Space **21** (2024) 131. https://doi.org/10.1016/j.undsp.2024.07.007
5 H. Sekiya, K. Masuda, S. Nagakura, and S. Inuzuka: Tunnelling Underground Space Technol. **126** (2022) 104535. https://doi.org/10.1016/j.tust.2022.104535
6 C. Y. Gue, M. Wilcock, M. M. Alhaddad, M. Z. E. B. Elshafie, K. Soga, and R. J. Mair: J. Civ. Struct. Health Monit. **5** (2015) 573. https://doi.org/10.1007/s13349-015-0109-8
7 H. Cui, X. Ren, Q. Mao, Q. Hu, and W. Wang: Autom. Constr. **106** (2019) 102889. https://doi.org/10.1016/j.autcon.2019.102889
8 H. Mohamad, K. Soga, P. J. Bennett, R. J. Mair, and C. S. Lim: J. Geotech. Geoenviron. Eng. **138** (2012) 957. https://doi.org/10.1061/(ASCE)GT.1943-5606.0000656
9 S. Mustafa, H. Sekiya, I. Maeda, S. Takaba, and A. Hamajima: Opt. Fiber Technol. **67** (2021) 102705. https://doi.org/10.1016/j.yofte.2021.102705
10 S. Mustafa, H. Sekiya, S. Morichika, I. Maeda, S. Takaba, and A. Hamajima: Opt. Fiber Technol. **68** (2022) 102829. https://doi.org/10.1016/j.yofte.2022.102829
11 L. Luo, H. Sekiya, and K. Soga: IEEE Sens. J. **19** (2019) 5639. https://doi.org/10.1109/JSEN.2019.2907889
12 S. M. Khan, M. U. Hanif, A. Khan, M. U. Hassan, A. Javanmardi, and A. Ahmad: Structures **41** (2022) 602. https://doi.org/10.1016/j.istruc.2022.04.101
13 S. Morichika, H. Sekiya, Y. Zhu, S. Hirano, and O. Maruyama: IEEE Sens. J. **21** (2021) 8204. https://doi.org/10.1109/JSEN.2021.3051697
14 K. M. Tsang and W. L. Chan :Measurement **44** (2011) 1201. https://doi.org/10.1016/j.measurement.2011.03.025
15 L. Zhu, Y. Fu, R. Chow, B. F. Spencer, J. W. Park, and K. Mechitov: Sensors **18** (2018) 262. https://doi.org/10.3390/s18010262
16 F. Zanelli, M. Marui, F. Castelli-Dezza, D. Tarsitano, A. Manenti, and G. Diana: Sensors **22** (2022) 8165. https://doi.org/10.3390/s22218165
17 T. Buckley, B. Ghosh, and V. Pakrashi: Sensors **21** (2021) 6760. https://doi.org/10.3390/s21206760
18 H. E. Ahmed, S. Sahandabadi, Bhawya, and M. J. Ahamed: Sensors **14** (2023) 923. https://doi.org/10.3390/mi14050923
19 P. A. Psimoulis and S. C. Stiros: J. Bridge Eng. **18** (2013) 182. https://doi.org/10.1061/(ASCE)BE.1943-5592.0000334
20 Y. Koto, T. Konishi, H. Sekiya, and C. Miki: J. Sound Vib. **438** (2019) 238. https://doi.org/10.1016/j.jsv.2018.09.009
21 Z. Ma, J. Choi, and H. Sohn: Eng. Struct. **292** (2023) 116535. https://doi.org/10.1016/j.engstruct.2023.116535
22 Z. Su, B. Wei, and J. Zhang: Autom. Constr. **154** (2023) 105008. https://doi.org/10.1016/j.autcon.2023.105008
23 Z. W. Chen, Q. L. Cai, and S. Zhu: Struct. Control Health Monit. **25** (2018) 1. https://doi.org/10.1002/stc.2242
24 S. Zhang and Y. Liu: Appl. Sci. **9** (2019) 1805. https://doi.org/10.3390/app9091805

25 Q. Cai, Z. Chen, and S. Zhu: J. Bridge Eng. **28** (2023) 04022151. https://doi.org/10.1061/JBENF2.BEENG-5893
26 L. Ge, K. Y. Koo, M. Wang, J. Brownjohn, and D. Dan: Eng. Struct. **288** (2023) 116185. https://doi.org/10.1016/j.engstruct.2023.116185
27 S. Mustafa, H. Sekiya, and S. Hirano: Structures **53** (2023) 1160. https://doi.org/10.1016/j.istruc.2023.04.126
28 M. Lydon, S. E. Taylor, D. Robinson, A. Mufti, and E. J. O. Brien: J. Civ. Struct. Health Monit. **6** (2016) 69. https://doi.org/10.1007/s13349-015-0119-6
29 Y. Yu, C. S. Cai, and L. Deng: Adv. Struct. Eng. **19** (2016) 1514. https://doi.org/10.1177/1369433216655922
30 S. Mustafa, I. Yoshida, and H. Sekiya: Structures **33** (2021) 2061. https://doi.org/10.1016/j.istruc.2021.05.082
31 M. Gindy, R. Vaccaro, H. Nassif, and J. Velde: Comput.-Aided Civ. Infrastruct. Eng. **23** (2008) 281. https://doi.org/10.1111/j.1467-8667.2007.00536.x
32 H. Sekiya, O. Maruyama, and C. Miki: Sens. Mater. **29** (2017) 117. https://doi.org/10.18494/SAM.2017.1420
33 H. Sekiya: J. Bridge Eng. **24** (2019) 04019063. https://doi.org/10.1061/(ASCE)BE.1943-5592.0001411
34 I. Yoshida, H. Sekiya, and S. Mustafa: ASCE-ASME J. Risk Uncertainty Eng. Syst. Part A: Civ. Eng. **7** (2021) 04021001. https://doi.org/10.1061/AJRUA6.0001118
35 I. Yoshida, S. Mustafa, K. Maruyama, and H. Sekiya: Struct. Saf. **103** (2023) 102350. https://doi.org/10.1016/j.strusafe.2023.102350
36 M. Zhang, S. Li, and P. Li: Comput. Geotech. **118** (2020) 103325. https://doi.org/10.1016/j.compgeo.2019.103325
37 J. Shi, F. Wang, D. Zhang, and H. Huang: Comput. Geotech. **137** (2021) 104312. https://doi.org/10.1016/j.compgeo.2021.104312
38 Y. Koyama: Tunnelling Underground Space Technol. **18** (2003) 145. https://doi.org/10.1016/S0886-7798(03)00040-3
39 H. Mashimo and T. Ishimura: Tunnelling Underground Space Technol. **18** (2003) 233. https://doi.org/10.1016/S0886-7798(03)00032-4
40 L. Z. Wang, Z. Wang, L. L. Li, and J. C. Wang: Tunnelling Underground Space Technol. **26** (2011) 674. https://doi.org/10.1016/j.tust.2011.05.009
41 A. M. M. Wood: Géotechnique **25** (1975) 115. https://doi.org/10.1680/geot.1975.25.1.115
42 Railway Technical Research Institute: Design Standard for Railway Structures and Commentary (Shield Tunnel) [Japanese Railway Technical Research Institute (RTRI), Tokyo, 2002].
43 W. M. Huang, J. C. Wang, Z. X. Yang, and R. Q. Xu: Tunnelling Underground Space Technol. **127** (2022) 104601. https://doi.org/10.1016/j.tust.2022.104601
44 C. Zhang, H. Zhang, M. Huang, and J. Yu: Comput. Geotech. **157** (2023) 105333. https://doi.org/10.1016/j.compgeo.2023.105333
45 O. Arnau and C. Molins: Tunnelling Underground Space Technol. **26** (2011) 778. https://doi.org/10.1016/j.tust.2011.04.005
46 P. Chaipanna and P. Jongpradist: Tunnelling Underground Space Technol. **90** (2019) 369. https://doi.org/10.1016/j.tust.2019.05.015